

A finite element model of cell deformation during magnetic bead twisting

SRBOLJUB M. MIJAILOVICH,¹ MILOS KOJIC,^{1,2}
MIROSLAV ZIVKOVIC,² BEN FABRY,¹ AND JEFFREY J. FREDBERG¹
¹Harvard School of Public Health, Boston, Massachusetts 02115;
and ²University of Kragujevac, 34000 Kragujevac, Yugoslavia

Received 27 March 2002; accepted in final form 17 June 2002

Mijailovich, Srboljub M., Milos Kojic, Miroslav Zivkovic, Ben Fabry, and Jeffrey J. Fredberg. A finite element model of cell deformation during magnetic bead twisting. *J Appl Physiol* 93: 1429–1436, 2002. First published June 21, 2002; 10.1152/jappphysiol.00255.2002.—Magnetic twisting cytometry probes mechanical properties of an adherent cell by applying a torque to a magnetic bead that is tightly bound to the cell surface. Here we have used a three-dimensional finite element model of cell deformation to compute the relationships between the applied torque and resulting bead rotation and lateral bead translation. From the analysis, we computed two coefficients that allow the cell elastic modulus to be estimated from measurements of either bead rotation or lateral bead translation, respectively, if the degree of bead embedding and the cell height are known. Although computed strains in proximity of the bead can be large, the relationships between applied torque and bead rotation or translation remain virtually linear up to bead rotations of 15°, above which geometrical nonlinearities become significant. This appreciable linear range stands in contrast to the intrinsically nonlinear force-displacement relationship that is observed when cells are indented during atomic force microscopy. Finally, these computations support the idea that adhesive forces are sufficient to keep the bead firmly attached to the cell surface throughout the range of working torques.

elastic modulus; cell stiffness; bead embedding; cell height; magnetic twisting cytometry

CELL DEFORMABILITY PLAYS AN important role in a variety of cell functions, including contraction, spreading, crawling, and wound healing (4–6, 13). To measure cell deformability and its changes, our laboratory has made extensive use of magnetic twisting cytometry (5, 6, 14, 15, 20, 22, 23, 29, 35, 37–39). Magnetic twisting cytometry probes mechanical properties of an adherent cell by applying a torque to a magnetic bead that is tightly bound to the cell surface. Most studies that use this method have reported the relationship between the applied torque and resulting angular rotations. More recent studies have reported the relationship between the applied torque and resulting lateral bead displacements (10, 11). With either approach, data analysis reported thus far has emphasized relative changes in

cell stiffness, or an “apparent stiffness,” rather than the absolute elastic modulus.

In this report, we have used three-dimensional finite element models to compute the relationships between the applied torque and resulting cell deformation, bead rotation, and lateral bead translation. We have assessed the effects of different degrees of bead embedding and cell height within a geometrically linear range of cell deformation. From these relationships, the elastic modulus of the cell can be computed if the bead-cell geometry is known. Assuming a linear elastic material and using geometrically nonlinear finite element analysis, we also assessed the limit up to which the linear analysis can be used.

METHODS

Finite Element Model, Boundary Conditions, and Model Parameters

Geometry. The cell was modeled as a three-dimensional slab with locally constant height and a lateral extent of 50 bead diameters (Fig. 1B). Justification for the assumption of a locally constant cell height is addressed in the DISCUSSION. We also considered a spherical bead embedded in an infinite elastic space that could be compared with an exact analytic solution (28).

Finite element formulation. The finite element program PAK (17, 19) was used to calculate the rotation and displacement of a rigid sphere partially or completely embedded in the deformable continuum (cell). The deformable continuum is defined as elastic solid of finite or semi-infinite thickness, with the bottom surface fixed to the rigid surface. For a torque applied along the *x*-axis (Fig. 1A), we calculated displacements, strains, and stresses within the material (i.e., cell) and also the bead translation and rotation. We assumed no slipping between the bead surface and the cell body at the interface.

The essence of the finite element method consists of division of a continuum into subdomains, called finite elements, in which an approximate displacement field \mathbf{u} is defined as

$$\mathbf{u} = \sum_k \mathbf{h}_k \mathbf{U}^k \quad (1)$$

where \mathbf{h}_k is the interpolation function (polynomial) and \mathbf{U}^k is the displacement vector of the *k*th finite element nodal point

Address for reprint requests and other correspondence: S. M. Mijailovich, Physiology Program, Dept. of Environmental Health, Bldg. I, Rm. 1306B, Harvard School of Public Health, 665 Huntington Ave., Boston, MA 02115 (E-mail: smijailo@hsph.harvard.edu).

The costs of publication of this article were defrayed in part by the payment of page charges. The article must therefore be hereby marked “advertisement” in accordance with 18 U.S.C. Section 1734 solely to indicate this fact.

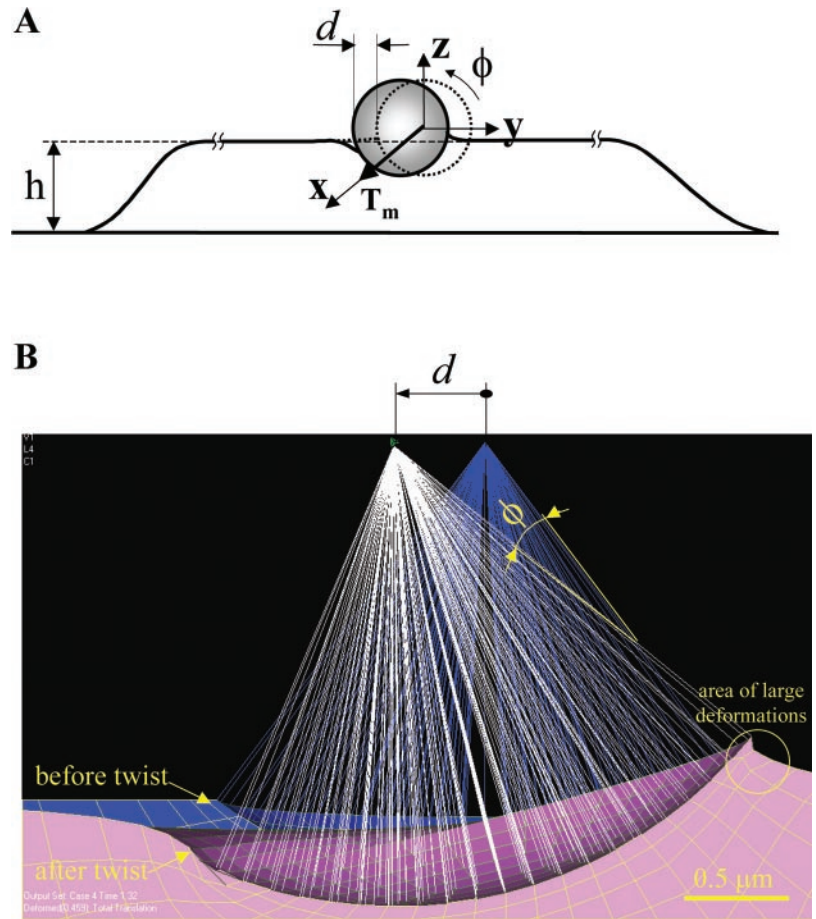


Fig. 1. Cell deformation and bead movement imposed by the magnetic twisting moment. **A**: schematic of oscillatory magnetic twisting cytometry. A homogeneous magnetic twisting field (acting in the vertical direction) causes the bead to rotate and to displace. T_m , applied magnetic torque; h , cell height. Magnetic twisting cytometry measures the angular rotation of the beads (ϕ) by detecting the horizontal component of the bead's remanent field (20, 36). Optical magnetic twisting cytometry measures bead lateral translation (d) by using a phase-synchronized video camera (10, 11). x , y , z : x -, y -, and z -axes. **B**: cell deformation predicted by the finite element model of 10% embedded bead. Before application of the magnetic twisting moment, the cell is undeformed (blue in the background). After application of magnetic field, cell deforms and bead simultaneously rotate (for angle ϕ) and laterally translate (for displacement d). Small vertical translation is not relevant to our study. The applied torque is at the limit of linear torque-rotation range of 15° . Note large deformations at the edge of the bead-cell interface, which sharply decrease toward the middle of the cell-bead interface.

(1). For given material constitutive relations, the global finite element equilibrium equations are obtained by assembling the individual finite element equilibrium equations for all elements within the discretized domain. The properly defined boundary conditions must also be included in the finite element model. First, the system of equations is solved for nodal displacements, and then displacements of the material points within each finite element are calculated from Eq. 1. The strains are obtained by the appropriate differentiations of the displacement field, whereas the stresses are calculated from these strains and the material constitutive relations.

We assumed that bead stiffness is much larger than cell stiffness, in which case, considering bead as a rigid body, the bead motion is defined by displacement of its center and its rotation. We impose the condition that displacements at the interface between the rigid bead (\mathbf{u}_{bead}) and the deformable cell (\mathbf{u}_{cell}) are the same

$$\mathbf{u}_{\text{bead}} = \mathbf{u}_{\text{cell}} \quad (2)$$

The torque applied to the bead is balanced by tractions at the bead-cell interface. These tractions are calculated from nodal forces at the cell-bead interface (2, 21).

In the finite element analysis, we used three-dimensional, solid, isoparametric, linear eight-node elements. Typically, the total number of nodes was $\sim 4,500$ with $\sim 15,000$ elements.

We performed two analyses; in both we assumed that the material was linearly elastic. The first analysis was geometrically linear in the sense that it did not take into account

geometrical distortions induced by bead motion. The second analysis was geometrically nonlinear in that it did take into account such distortions. To do this latter analysis, we included quadratic terms in the strain calculations and change of geometry. Thus the Cauchy (true) stresses were related to the Almansi strains in the linear constitutive law.

We used a Poisson ratio, $\nu = 0.49$, a value that does not cause pressure locking of the elements. We also performed calculations with $\nu = 0.45$ and 0.499 and found only minor changes in sphere rotation and displacement (differences of $< 0.5\%$). The stress field corresponding to $\nu = 0.49$ was altered by only a few percent in the case when ν was equal to 0.45 . Thus our calculations with $\nu = 0.49$ are reasonably accurate.

The finite element mesh. We point out that the stress everywhere on the bead-cell interface is expected to be bounded. This result is nontrivial, biologically important, and impacts the question of what is a sufficiently fine mesh for reasonable finite element approximations. The stress is bounded, even at the extremes of the bead-cell interface, because the sphere acts on the deformable cell as a rigid body without sharp edges (24). This is in contrast to the case of a rigid punch with sharp edges, which causes infinite stresses in elastic deformable solid in the proximity of the punch edges.

In the case of a bead embedded by only 10% of its diameter, we performed calculations with two meshes, one of which had 50% more elements than the other. In regions of maximum stress, we found differences approaching $\sim 2.5\%$, with much

smaller discrepancies elsewhere. The corresponding differences in computed bead displacements and rotations were <0.1%. Thus the use of the finer mesh was not necessary.

The dependency of the results on the mesh size in the regions of high deformations is important, however, in analysis of geometrical nonlinearities. We observed negative Jacobians (i.e., the determinant of the transformation matrix between Cartesian and isoparametric coordinates) in a few of the most distorted elements when bead rotation exceeded 15°. An extreme case, in which Jacobians are still positive but small, is shown in Fig. 1B. The contribution of these distorted elements to the overall response was negligible, however. In the linear analysis, the Jacobians remained constant and are independent of the element distortion; in that case, we limited our calculations to specific torques (T_s) that were 25% smaller than those used in the nonlinear analysis. Numerical computations for the case of a bead embedded in an infinite medium (Fig. 2A) agreed within 0.5% with the corresponding analytic solution of Phan-Thien (28).

Parameter values. The diameter of the ferromagnetic bead was taken as 4.5 μm . The elastic material parameters of the deformable continuum (i.e., the cell) were taken as shear modulus (G) = 1,000 Pa and $\nu = 0.49$; the G is related to the Young's

modulus (E) by the relationship $G = E/[2(1 + \nu)]$. We studied beads embedded to a depth of 5, 10, 25, 75, and 100% of the bead diameter, and cell heights of 1 and 5 μm and semi-infinite.

Two different definitions for T_s have been used in the literature, and they differ by geometric scaling factor (6 for spherical beads) (10, 11, 20, 36, 38). Here we follow Fabry et al. (10, 11) by defining T_s as applied magnetic torque (T_m) per unit of bead volume. For the linear finite element analysis, the T_s acting on the bead is taken to be $T_s = 60$ Pa.

Calculation of Apparent Cell Stiffness from Measured Rotation or Lateral Translation

The magnetic twisting field (i.e., the applied magnetic moment) causes both a rotation and a lateral translation of the beads (Fig. 1). The bead rotation is ϕ , and the normalized lateral translation is $d^* = d/R$ [i.e., the bead lateral translation, d , expressed as a fraction of the bead radius (R)]. We define apparent cell stiffness as $G_\phi = T_s/(\kappa\phi)$ obtained from the bead rotation, or apparent cell stiffness as $G_d = T_s/(\kappa d^*)$ from the bead lateral translation. Here κ is a shape factor (6 for spherical beads). We will show below that G_ϕ and G_d

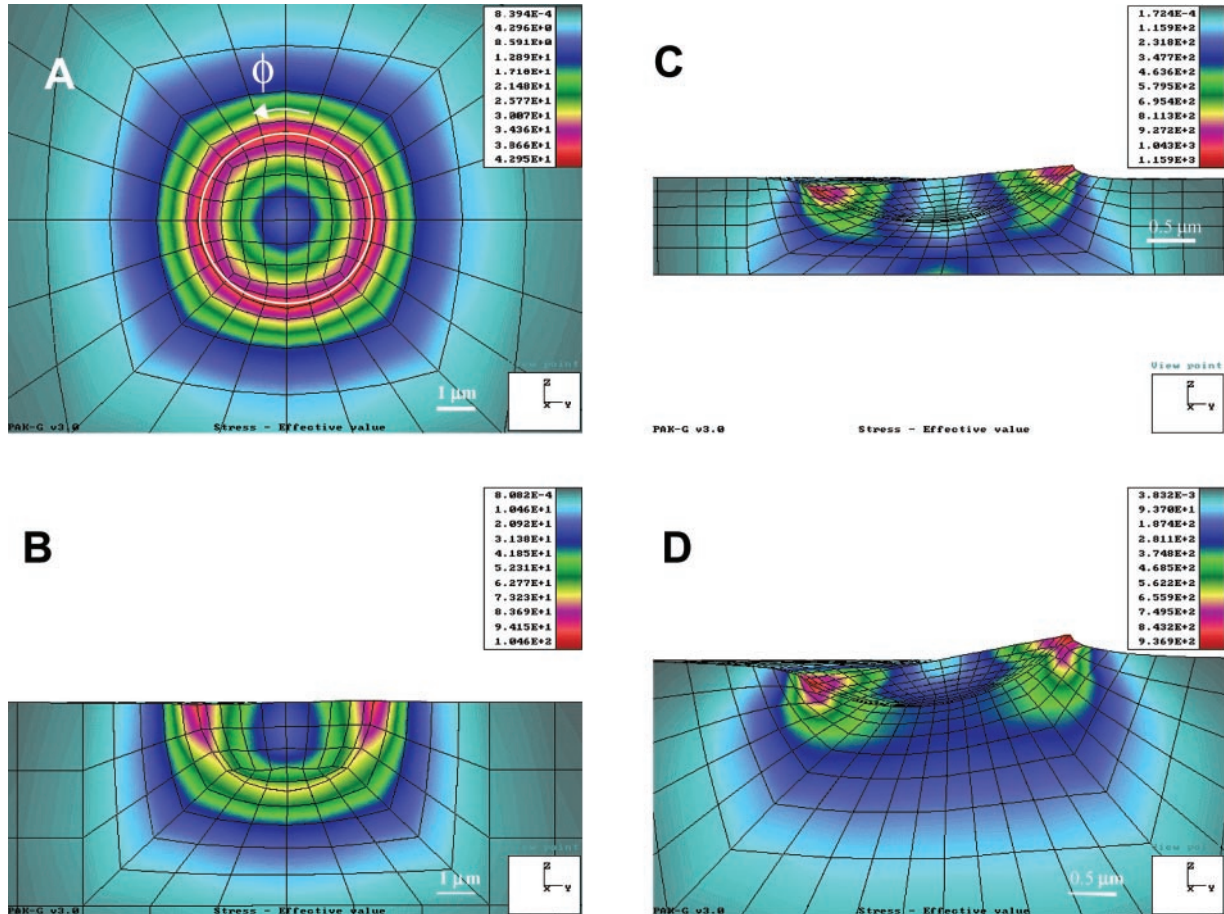


Fig. 2. Deformed shapes of cell subjected to magnetic twisting torque and the corresponding equivalent (von Mises) stress fields for the representative cases of the embedded bead in the cell or attached on the cell surface. The stress shown is in Pa. Von Mises stress is defined as $\bar{\sigma} = \sqrt{3/2 S_{ij} \cdot S_{ij}}$, where $S_{ij} = \sigma_{ij} - 1/3 \sigma_{kk} \delta_{ij}$; $i, j = 1, 2, 3$ are components of stress deviator; and σ_{ij} are stress components in Cartesian system x_i (i.e., x, y, z). Stress is shown in the plane passing through the bead center. A: bead embedded in an infinite medium. Cell surface behind the plane is shown within the white circle. B: bead 50% embedded in 5- μm -high cell. C: bead 10% embedded in 1- μm -high cell. D: bead 10% embedded in 5- μm -high cell.

strongly depend on the degree of bead internalization and to a lesser degree on the cell height.

We calculated the relationship between the cell G and the apparent stiffnesses G_ϕ and G_d from torque-rotation and torque-displacement dependencies obtained in our analysis. We defined coefficients α and β by the relationships $G_\phi = \alpha G$ and $G_d = \beta G$ and then computed α and β each as a function of the depth of bead embedding and cell height.

RESULTS

Deformation, Stress, and Traction

Cell deformation and the stress fields in the plane perpendicular to the magnetic torque passing through the center of the bead are shown for four representative cases (Fig. 2). In all cases, the bead is taken out of the view, but the stresses at the cell-bead interface are shown. We show the equivalent (von Mises) stress (1), which is the overall measure of maximum shear stress. The simplest case is rotation about the x -axis of a bead in an infinite medium (Fig. 2A). In this case, there is no bead translation: the strain and stress fields and the interfacial tractions are uniform along the circumference in the plane perpendicular to the T_m . Stress decays rapidly in the radial direction (i.e., $\sim R/r^3$), from the maximum value at cell-microbead interface to $\sim 15\%$ of that value at the radial distance of $\sim 2 \mu\text{m}$ from the microbead surface. Stress at the bead-cell interface (shown inside the white circle in Fig. 2A) decays to zero at the central point that lies on the spherical surface and the center of the axis of rotation. The maximum value of the interfacial traction is in the plane passing through the center of the bead; for a bead twisted by a T_s of 60 Pa, the traction is equal to 30 Pa.

In contrast to the case of a bead in an infinite space, for a bead 50% embedded in a cell $5 \mu\text{m}$ in height (Fig. 2B), the stress distribution is highly nonuniform around the bead interface and is maximal near the intersection of the bead and the free apical surface of the cell. This stress nonuniformity is far more prominent when the bead is only 10% embedded (Fig. 2, C and D, for two different cell heights). For 50% embedding, the peak stress is about two times larger than that of the bead immersed in an infinite medium, whereas for 10% embedding, the peak stress is >25 times larger. Moreover, reduction of cell height from 5 to $1 \mu\text{m}$ (Fig. 2, C and D) further increases the peak stresses by $\sim 20\%$. The maximum stress is at the bead surface and coincides with maximum traction at the cell-bead interface. The maximum tractions also increase rapidly for less embedded beads. For example, for 10% embedding, the maximum traction is $\sim 2.5 \text{ kPa}$ (Fig. 3). The effect of these local peak stresses and peak tractions at the bead-cell interface is discussed below.

Cell Shear Modulus

Figure 4A shows the relationship between the coefficient α and the degree of bead embedding for three different cell heights. With less bead embedding, α is much smaller than 1. For example, for 10% embedding,

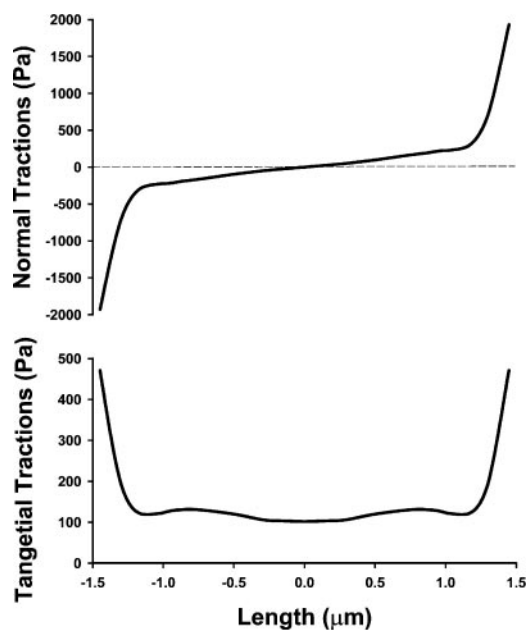


Fig. 3. Normal and tangential tractions along bead-cell interface in the plane passing through the bead center, for 10% embedded bead, h of $5 \mu\text{m}$ (as shown in Fig. 2D), applied specific torque of 60 Pa and cell shear modulus of 1,000 Pa. In this case, ϕ is $\sim 11.5^\circ$.

G_ϕ is only 5% of G (Fig. 4A), but α increases toward unity as bead embedding increases. A decrease of the cell height below one-half of the microbead diameter at fixed bead embedding increases α more significantly, because the smaller bead rotation is caused by greatly reduced cell deformation in proximity of the rigid substrate.

Figure 4B shows the relationship between the coefficient β and the degree of bead embedding for three different cell heights. Interestingly, the values of β are only slightly larger than α for the small degrees of bead embedding, but they become progressively larger than α as bead embedding increases. For a large degree of embedding ($>70\%$), β becomes much larger than 1 and unbounded for the bead embedded in an infinite medium, whereas α never exceeds 1. These differences in α vs. β for the same degree of microbead embedding follows from the fact that, for the completely immersed microbead, the rotation remains finite, whereas the lateral displacement approaches zero.

The coefficients α and β decrease progressively when the cell height decreases below one bead diameter but change relatively little when the cell height is larger than one bead diameter (Fig. 4).

Nonlinearity

Partially embedded beads show stress concentrations and associated large local deformations (Fig. 2, C and D). For example, the maximum strain for 10% embedded bead may reach 30% at $T_s = 60 \text{ Pa}$ and up to 50% at $T_s = 80 \text{ Pa}$ (Fig. 5). These maximum strain values are much larger than the usual small deformation limit of 4% (1, 18). Moreover, these large deforma-

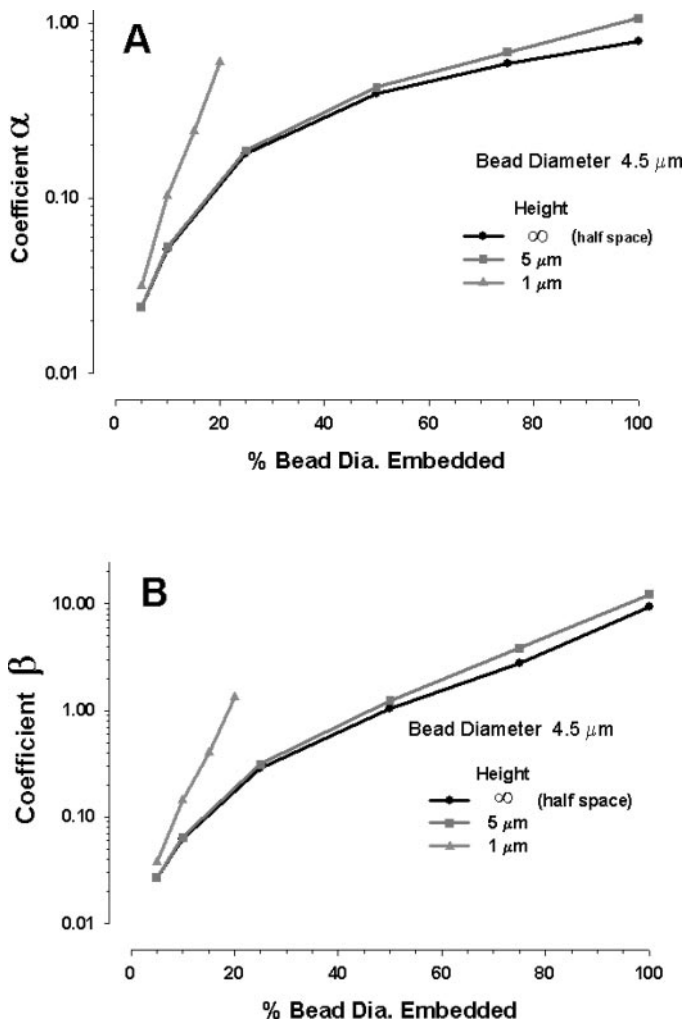


Fig. 4. Computed coefficients α and β (see METHODS for definitions), as functions of the degree of bead embedding and h . A: coefficient α (related to ϕ) vs. degree of bead embedding and h . In this case, the sphere embedded in infinite elastic medium $\alpha = 1$, i.e., apparent cell shear stiffness (G_ϕ), is equal to cell elastic shear modulus (G). B: coefficient β (related to bead translation $d^* = d/R$, where R is bead radius) vs. degree of bead embedding and h .

tions create geometrical nonlinearities. To our surprise, the nonlinear analysis (performed for 10% embedded bead) showed that the relationship between the T_s and the bead rotation and/or bead displacements is insensitive to these local geometrical nonlinearities and remains virtually linear up to a rotation angle $\phi = 15^\circ$. For $\phi > 15^\circ$, geometrical nonlinearities became significant.

DISCUSSION

Magnetic twisting cytometry probes mechanical properties of an adherent cell by applying a torque to a magnetic microbead that is tightly bound to the cell surface. Here we computed coefficients α and β that allow the cell elastic modulus to be estimated from measurements of either bead rotation or lateral bead translation, respectively, if the applied torque, the de-

gree of bead embedding, and the cell height are known. In the DISCUSSION, we deal first with three important limitations of the computational model and then go on to discuss the implication of our results.

First, this theoretical analysis of cell deformation is based on a highly simplified geometry of a spherical bead partially embedded in a homogeneous isotropic linear elastic slab whose height is locally uniform. Real cell geometry is, of course, far more complex (40), with cell height varying along and across the adherent cell. The analysis shows, however, that fields of stress and strain induced by the imposed torque decay rapidly in the radial direction, varying roughly as the inverse cube of distance from the bead; within one bead diameter, the stress and strain become quite small (Figs. 2 and 5). This highly localized response implies that geometrical details at lateral distances of more than one bead diameter would be expected to have at most only a slight influence on the computed results. Therefore, the analysis would be expected to be valid for regions in which changes of cell height are small over distances comparable to one bead diameter.

Second, to perform these calculations, we used only one value for the G , a realistic one, but the results are applicable, nonetheless, for any value of the G . In the linear case, the assumed value of the G acts merely as a simple scale factor, setting the level of the stress field relative to that of the strain field. For a fixed applied torque, the stresses and tractions depend on the particular numerical value of the modulus. Note that spatial distribution of strains depends neither on the applied torque nor on the modulus. Much the same is true in the case of induced nonlinear distortions: the angular rotations required to induce a geometric nonlinearity would be unchanged, but the level of the torque required to induce that rotation would change.

Third, the computational analysis reported here was limited to static conditions and does not explicitly take into account dynamic properties of the cytoskeletal lattice, which could cause both frequency dependence of the elastic modulus and an appreciable loss modulus corresponding to internal frictional stresses (10). Before, we defined $G_\phi = \alpha G$ and $G_d = \beta G$, and now we define the complex moduli $\tilde{G}_\phi(f)$, $\tilde{G}_d(f)$, and $\tilde{G}(f)$, where f is the frequency of the excitation. These moduli denote complex variables possessing real (in-phase or elastic) components and imaginary (out-of-phase or frictional) components. Assuming that the cytoskeletal material is linear and incompressible, the computed results can be generalized such that $\tilde{G}_\phi(f) = \alpha \tilde{G}_\phi(f)$ and $\tilde{G}_d(f) = \beta \tilde{G}_d(f)$. The coefficients α and β are independent of frequency, and they are identical to the coefficients shown in Fig. 4. It can be shown that these coefficients equally apply to the cell constitutive law that obeys linear structural damping (8–10, 12) or linear viscoelasticity. The analysis should not be expected to extend to the case of plastic responses, however.

The key relationships for coefficients α and β are shown in Fig. 4. These relationships are counterintui-

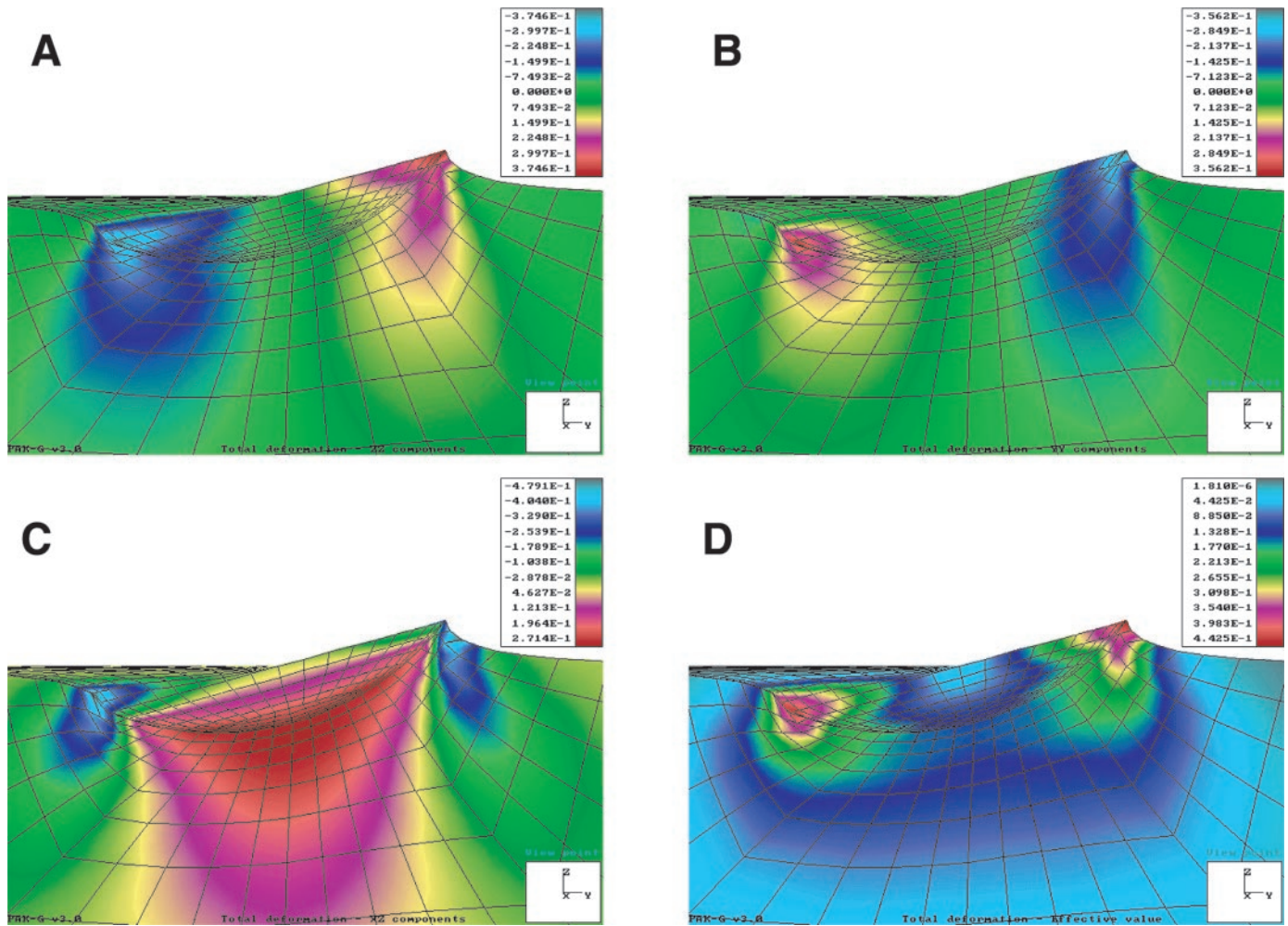


Fig. 5. Deformed shapes and strain fields in a cell 5 μm in height for bead embedded 10% of its diameter and ϕ of 15°. Shown are strain fields of the components of strain: ϵ_{zz} (A), ϵ_{yy} (B), ϵ_{yz} (C), and the effective strain ϵ_{eff} (D). The effective strain is defined as: $\epsilon_{\text{eff}} = \sqrt{2/3}\epsilon_{ij}\epsilon_{ij}$, where ϵ_{ij} are strain components in Cartesian system x_i (i.e., x, y, z).

tive in an important regard that deserves special comment. The results shown in Fig. 4 are surprisingly insensitive to cell height. For example, the results for infinite cell height vs. those for 5- μm cell height show only negligible differences for a small extent of bead embedding and, at most, only modest differences for 100% bead embedding. In the latter case (100% embedding of a 4.5- μm bead in a 5- μm thick slab), there is a rigid substrate with a no-slip boundary condition only 0.5 μm below the bead. It might have been thought that such close proximity of the rigid substrate would severely constrain bead motion and to an extent that is far greater than the analysis actually predicts. The analysis shows, however, that the dominant parts of the normal and tangential tractions that balance the torque applied to the bead are generated well away from the regions that most closely approach the rigid substrate (Fig. 3), thus resolving the paradox. However, the effect of the proximity of the rigid substrate becomes important when cell height is below one-half of bead diameter.

The coefficients α and β (Fig. 4) allow calculation of the cell elastic modulus from either torque-angle or torque-displacement measurements. The elastic modulus obtained in that way is comparable to the modulus obtained by other techniques. For example, the apparent cell stiffness of 60–100 Pa observed in smooth muscle cells (20) divided by the coefficient $\alpha = 0.1$ (that corresponds to average bead embedding of 20%) gives a cell G in the range of 600–1,000 Pa, which is comparable to measurements of the G of fibroblasts by micropipette manipulation (34) and cell poking (27). A similar value of the G is observed in myocytes obtained by atomic force microscopy (32). Similarly, an apparent shear cell stiffness of endothelial cells of ~ 10 Pa (38) divided by the same coefficient (0.1) becomes close to the G obtained from the micropipette aspiration measurements of ~ 100 Pa (30, 31).

The analysis shows that the degree of bead embedding and the cell height profoundly influence bead rotation and translation. Therefore, observed variations of bead embedding, cell height variation with

position of the bead on each cell (i.e., close to nucleus, where the smooth muscle cell height is $>5 \mu\text{m}$, and at the cell periphery where the cell height of the well-spread cell is $<2 \mu\text{m}$), may be the major factors contributing to the variability of the apparent stiffnesses calculated from the observed displacements of the individual bead displacements (10, 11). However, this variability can also be caused, at least in part, by differences in bead attachments to the cytoskeleton, by local stiffness differences within a cell, or differences between cells (different levels of activation, for example) that collectively contribute to the observed heterogeneity of apparent stiffness.

Our analysis gives a basis for an estimation of the range of linearity of the torque-rotation relationship over a wide range of bead embedding. In continuum mechanics of linear elastic solids, large deformations usually induce significant nonlinearity in the stress-strain relation for strains $>4\%$ (1, 18). Note that a strain of 4% corresponds to a bead rotation in an infinite medium of only 1.5° . Surprisingly, we found that, in the case of 10% embedding, the torque-rotation relationship remains linear up to a bead rotation of 15° or lateral translation of 20% of the bead radius, which, for a radius of $2.25 \mu\text{m}$, yields a lateral translation of $\sim 450 \text{ nm}$. This finding is consistent with experimentally observed linear rheological behavior among smooth muscle cells (10, 11). Although the maximum local strains approach 50%, which greatly exceeds the ordinary linearity limit of 4%, the region of these large strains is quite localized to the edges of the cell-bead interface (Fig. 5), and, as such, the overall system response remains virtually linear. With an increase of degree of bead embedding, these regions of large strains are less localized, and the linear torque-rotation limit must be gradually decreased (from bead rotation of 15° at 10% embedding to bead rotation of 1.5° in an infinite medium), regardless of a large decrease in the peak strains and stresses (Fig. 2). Despite this decrease of the linear limit, the maximum bead rotation of 15° is a sufficient criterion to ensure that a population of beads embedded $>10\%$ is within the linear torque-rotation range.

The existence of an appreciable linear range using this method stands in contrast to the force-displacement relationship measured with atomic force microscopy, which exhibits no linear range due to intrinsic geometric distortions induced by contact of the probe tip with the cell (7).

It is important to note that the bead lateral translations become extremely small for large-bead embedding (Fig. 6). For example, in the limit of the resolution of optical readings of $\sim 5 \text{ nm}$ (10, 11), the displacement (of $4.5\text{-}\mu\text{m}$ bead) can be accurately measured for beads embedded $<75\%$. Moreover, determination of dynamic moduli from torque-displacement loops may further be limited by the optical resolution to beads embedded $<50\%$.

Finally, in the literature, the interpretation of data obtained by magnetic twisting cytometry has rested on

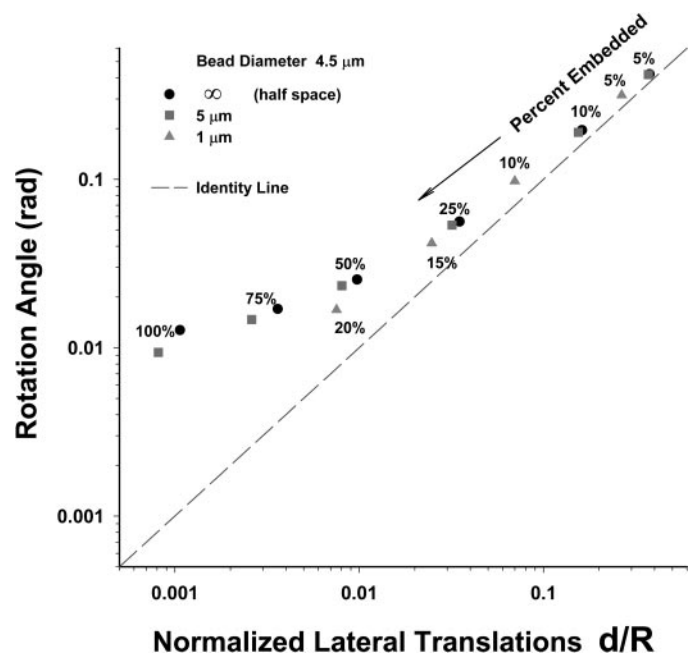


Fig. 6. Relationship between ϕ vs. d normalized by R for various degrees of the bead embedding and adherent h .

the assumption that receptor-ligand bonds have sufficient adhesion strength and numbers to keep the bead attached to the cell over the whole interface and ensure a no-slip boundary condition. Based on the tractions computed here, is that a reasonable assumption? Typical receptor-ligand bond strength is 10 pN, and a typical receptor-ligand bond density has a range from several hundred up to $10,000 \text{ bonds}/\mu\text{m}^2$ (3, 16, 25, 26, 41, 42). To support induced translation due to bead twisting, the minimum receptor density for the completely embedded bead (Fig. 2A) is only $3 \text{ bonds}/\mu\text{m}^2$, whereas, for a bead emerged 10%, the minimum required bond density may reach $>250 \text{ bonds}/\mu\text{m}^2$. Therefore, the ligand adhesion strength may be sufficient to keep the bead firmly attached to the cell and the cell to the substrate. Consequently, peeling of the bead from cell surface or the cell from substrate would not be expected to occur (10, 11, 20).

Conclusions

We have shown that the elastic modulus can be obtained from the apparent cell stiffness if the degree of bead embedding and cell height is known. The elastic modulus estimated in this way is consistent with estimates of the elastic modulus assessed by other techniques in muscle and nonmuscle cells (20, 33, 43). We have calculated the limiting maximum angle of rotation in terms of the degree of the bead embedding, for which the torque-angle of rotation and torque-displacement relationships are linear. Finally, based on estimated bond densities and maximum T_s values that are used in these techniques, we found that the adhesion strength of integrin bonds seems to be sufficient to keep the bead firmly attached to the cell.

We gratefully acknowledge Dr. Ning Wang and Dr. James Butler for helpful discussions and critical review of this article.

This work was supported by National Heart, Lung, and Blood Institute Grants HL-33009 and HL-59682.

REFERENCES

1. **Bathe KJ.** *Finite Element Procedures.* Englewood Cliffs, NJ: Prentice-Hall, 1996.
2. **Bathe KJ and Mijailovich SM.** Finite element analysis of frictional contact problems. *Journal de Mechanique et Applique* 7, Suppl 1–7: 31–47, 1988.
3. **Bell GI.** Models for the specific adhesion of cells to cells. *Science* 200: 618–627, 1978.
4. **Bereiter-Hahn J, Karl I, Luers H, and Voth M.** Mechanical basis of cell shape: investigations with the scanning acoustic microscope. *Biochem Cell Biol* 73: 337–348, 1995.
5. **Chen CS, Mrksich M, Huang S, Whitesides GM, and Ingber DE.** Geometric control of cell life and death. *Science* 276: 1425–1428, 1997.
6. **Chicurel ME, Singer RH, Meyer CJ, and Ingber DE.** Integrin binding and mechanical tension induce movement of mRNA and ribosomes to focal adhesions. *Nature* 392: 730–733, 1998.
7. **Costa KD and Yin FC.** Analysis of indentation: implications for measuring mechanical properties with atomic force microscopy. *J Biomech Eng* 121: 462–471, 1999.
8. **Crandall SH.** Dynamic response of systems with structural damping. In: *Air, Space, and Instruments. Draper Anniversary Volume*, edited by Lees S. New York: McGraw-Hill, 1963, p. 183–193.
9. **Crandall SH.** The role of damping in vibration theory. *J Sound Vib* 13: 3–18, 1970.
10. **Fabry B, Maksym GN, Butler JP, Glogauer M, Navajas D, and Fredberg JJ.** Scaling the microrheology of living cells. *Physiol Rev Lett* 87: 148102, 2001.
11. **Fabry B, Maksym GN, Shore SA, Moore PE, Panettieri RA Jr, Butler JP, and Fredberg JJ.** Selected contribution: time course and heterogeneity of contractile responses in cultured human airway smooth muscle cells. *J Appl Physiol* 91: 986–994, 2001.
12. **Fredberg JJ and Stamenovic D.** On the imperfect elasticity of lung tissue. *J Appl Physiol* 67: 2408–2419, 1989.
13. **Galbraith CG, Skalak R, and Chien S.** Shear stress induces spatial reorganization of the endothelial cell cytoskeleton. *Cell Motil Cytoskeleton* 40: 317–330, 1998.
14. **Hubmayr RD, Shore SA, Fredberg JJ, Planus E, Panettieri RA Jr, Moller W, Heyder J, and Wang N.** Pharmacological activation changes stiffness of cultured human airway smooth muscle cells. *Am J Physiol Cell Physiol* 271: C1660–C1668, 1996.
15. **Ingber DE.** Tensegrity: the architectural basis of cellular mechanotransduction. *Annu Rev Physiol* 59: 575–599, 1997.
16. **Irvine DJ, Hue KA, Mayes AM, and Griffith LG.** Simulations of cell-surface integrin binding to nanoscale-clustered adhesion ligands. *Biophys J* 82: 120–132, 2002.
17. **Kojic M.** The governing parameter method for implicit integration of viscoplastic constitutive relations for isotropic and orthotropic metals. *Int J Computational Mechanics* 19: 49–57, 1996.
18. **Kojic M and Bathe KJ.** *Inelastic Analysis of Solids and Structures.* Heidelberg, Germany: Springer-Verlag. In press.
19. **Kojic M, Grujovic N, Slavkovic R, and Zivkovic M.** A general orthotropic von Mises plasticity material model with mixed hardening—model definition and implicit stress integration procedure. *Trans ASME* 63: 376–382, 1996.
20. **Maksym GN, Fabry B, Butler JP, Navajas D, Tschumperlin DJ, Laporte JD, and Fredberg JJ.** Mechanical properties of cultured human airway smooth muscle cells from 0.05 to 0.4 Hz. *J Appl Physiol* 89: 1619–1632, 2000.
21. **Mijailovich SM, Stamenovic D, and Fredberg JJ.** Toward a kinetic theory of connective tissue micromechanics. *J Appl Physiol* 74: 665–681, 1993.
22. **Moore PE, Lahiri T, Laporte JD, Church T, Panettieri RA Jr, and Shore SA.** Signal Transduction in Smooth Muscle: Selected Contribution: Synergism between TNF- α and IL-1 β in airway smooth muscle cells: implications for β -adrenergic responsiveness. *J Appl Physiol* 91: 1467–1474, 2001.
23. **Moore PE, Laporte JD, Abraham Schwartzman IN, JH, Yandava CN, Silverman ES, Drazen JM, Wand MP, Panettieri RA Jr, and Shore SA.** Polymorphism of the beta(2)-adrenergic receptor gene and desensitization in human airway smooth muscle. *Am J Respir Crit Care Med* 162: 2117–2124, 2000.
24. **Muskhelishvili NI.** *Some Basic Problems of the Mathematical Theory of Elasticity.* Groningen, Holland: Noordhoff, 1953.
25. **Needham D and Nunn RS.** Elastic deformation and failure of lipid bilayer membranes containing cholesterol. *Biophys J* 58: 997–1009, 1990.
26. **Noppl-Simons DA and Needham D.** Avidin-biotin interactions at vesicle surfaces: adsorption and binding, cross-bridge formation, and lateral interactions. *Biophys J* 70: 1391–1401, 1996.
27. **Petersen NO, McConnaughey WB, and Elson EL.** Dependence of locally measured cellular deformability on position on the cell, temperature, and cytochalasin B. *Proc Natl Acad Sci USA* 79: 5327–5331, 1982.
28. **Phan-Thien N.** Rigid spherical inclusion: the multiple expansion. *J Elast* 32: 243–252, 1993.
29. **Potard US, Butler JP, and Wang N.** Cytoskeletal mechanics in confluent epithelial cells probed through integrins and E-cadherins. *Am J Physiol Cell Physiol* 272: C1654–C1663, 1997.
30. **Sato M, Ohshima N, and Nerem RM.** Viscoelastic properties of cultured porcine aortic endothelial cells exposed to shear stress. *J Biomech* 29: 461–467, 1996.
31. **Sato M, Theret DP, Wheeler LT, Ohshima N, and Nerem RM.** Application of the micropipette technique to the measurement of cultured porcine aortic endothelial cell viscoelastic properties. *J Biomech Eng* 112: 263–268, 1990.
32. **Shroff SG, Saner DR, and Lal R.** Dynamic micromechanical properties of cultured rat atrial myocytes measured by atomic force microscopy. *Am J Physiol Cell Physiol* 269: C286–C292, 1995.
33. **Stamenovic D and Coughlin MF.** The role of prestress and architecture of the cytoskeleton and deformability of cytoskeletal filaments in mechanics of adherent cells: a quantitative analysis. *J Theor Biol* 201: 63–74, 1999.
34. **Thoumine O and Ott A.** Time scale dependent viscoelastic and contractile regimes in fibroblasts probed by microplate manipulation. *J Cell Sci* 110: 2109–2116, 1997.
35. **Valberg PA.** Magnetometry of ingested particles in pulmonary macrophages. *Science* 224: 513–516, 1984.
36. **Valberg PA and Butler JP.** Magnetic particle motions within living cells. Physical theory and techniques. *Biophys J* 52: 537–550, 1987.
37. **Wang N, Butler JP, and Ingber DE.** Mechanotransduction across the cell surface and through the cytoskeleton. *Science* 260: 1124–1127, 1993.
38. **Wang N and Ingber DE.** Control of cytoskeletal mechanics by extracellular matrix, cell shape, and mechanical tension. *Biophys J* 66: 2181–2189, 1994.
39. **Wang N and Ingber DE.** Probing transmembrane mechanical coupling and cytomechanics using magnetic twisting cytometry. *Biochem Cell Biol* 73: 327–335, 1995.
40. **Wang N, Naruse K, Stamenovic D, Fredberg JJ, Mijailovich SM, Tolic-Norrelykke IM, Polte T, Mannix R, and Ingber DE.** Mechanical behavior in living cells consistent with the tensegrity model. *Proc Natl Acad Sci USA* 98: 7765–7770, 2001.
41. **Ward MD, Dembo M, and Hammer DA.** Kinetics of cell detachment: effect of ligand density. *Ann Biomed Eng* 23: 322–331, 1995.
42. **Ward MD and Hammer DA.** A theoretical analysis for the effect of focal contact formation on cell-substrate attachment strength. *Biophys J* 64: 936–959, 1993.
43. **Yamada S, Wirtz D, and Kuo SC.** Mechanics of living cells measured by laser tracking microrheology. *Biophys J* 78: 1736–1747, 2000.